Attosecond spectroscopy in condensed matter

Supplementary Information

A. L. Cavalieri[1], N. Müller[2], Th. Uphues[1,2], V. S. Yakovlev[3], A. Baltuška[1,4], B. Horvath [1], B. Schmidt[5], L. Blümel[5], R. Holzwarth[5], S. Hendel[2], M. Drescher[6], U. Kleineberg[3], P. M. Echenique[7], R. Kienberger[1], F. Krausz[1,3] & U. Heinzmann[2]

[1]*Max-Planck-Institut für Quantenoptik , Hans-Kopfermann-Str. 1, D-85748 Garching, Germany*

[2]*Fakultät für Physik, Universität Bielefeld, D-33615 Bielefeld, Germany*

[3]*Department für Physik, Ludwig-Maximilians-Universität, Am Coulombwall 1, D-85748 Garching, Germany*

[4]*Institut für Photonik, Technische Universität Wien, Gußhausstr. 27, A-10 40 Wien, Austria*

[5]*Menlo Systems GmbH, Am Klopferspitz 19, D-82152 Martinsried, Germany*

[6]*Institut für Experimentalphysik, Universität Hamburg, Luruper Chaussee 1 49, D-22761 Hamburg, Germany*

[7]*Dpto. Fisica de Materiales UPV/EHU, Centro Mixto CSIC-UPV/EHU and Donostia International Physics Center (DPIC), Paseo Manual de Lardizabal 4, 20018 San Sebastian, Spain*

Experimental Apparatus

The 1kHz repetition-rate, waveform-controlled, few-cycle, ~5-femtosecond, 400-μJ, 750-nm Ti:Sapphire laser system described by Baltuska *et. al.*[1,2] and Kienberger *et. al.*[3] is used in this experiment to generate both pump and probe pulses in our attosecond time-resolved photoelectron spectroscopy. Linearly polarized laser pulses are focused using a 500 mm focal length focusing optic into a Ne gas jet to produce high-harmonic (HH) radiation extending to the cut-off region near 90 eV. The interaction length in the Ne gas is ~2 mm. While the harmonic spectrum is structured in the region containing low order harmonics, in the cut-off region this structure vanishes when phase-stabilized few-cycle laser pulses with a near cosine-shaped waveform are employed as a driver. The carrier-envelope phase (CEP) of the pulses is chosen and held constant throughout our measurements to deliver cosine-carrier waveform pulses at the Ne gas jet. The CEP phase stability was maintained with measured fluctuations of ~0.1 rad rms throughout our measurements. Under these conditions, a single XUV pulse is created by isolating the cut-off region of the harmonic spectrum.

After generation of the HH spectral components, the XUV radiation and driver pulse co-propagate inside a differential vacuum pumping stage, which is used to isolate residual background Ne gas from the measurement chamber. The HH-generation chamber is further isolated from the experiment chamber by a Zr/pellicle assembly, which is installed in a vacuum gate valve. The pellicle assembly is also used to separate the XUV radiation from the near-infrared (NIR) driver pulse. The centre of the pellicle was replaced with a 150 nm Zr foil (5 mm diameter) which transmits ~60% of the XUV radiation in the cut-off region of the spectrum, but blocks the NIR driver pulse. Meanwhile, the remaining polymer membrane in the outer portion of the pellicle blocks the XUV radiation and transmits the NIR, which is later used as a streaking pulse.

Due to its isolation by differential pumping and the zirconium/pellicle assembly, the measurement chamber can be maintained under ultrahigh vacuum (UHV) conditions with typical background pressures $<10^{-9}$ mbar even though the background pressure in the HH chamber is typically $>10^{-2}$ mbar. With these UHV conditions in the measurement chamber, contamination of the crystal surface is minimized such that the 4*f*-band photoemission remains strongly peaked for ~3 hrs before the crystal must be cleaned. To clean the tungsten, it is retracted into a separate preparation chamber where it is heated in front of an oxygen doser to ~1400 K, followed by repeated flash heating to above 2200 K. Just after this procedure, the tungsten crystal surface is free of contaminants. The manipulator used for transport between the preparation and measurement chamber is also used to adjust the crystal position and orientation with respect to the incident XUV and NIR radiation.

Data Collection & Systematic Error

To minimize systematic experiment error, the 40 individual streaked spectra, which were combined to form the ATR spectrogram displayed in Fig. 2 of the main paper, were not collected in a single, sequential time scan. Instead, two measurement sets were collected, one with increasing relative-delay and the other with decreasing delay both sets started with relative delay near time zero, as defined by the overlap of the maximums of the NIR and XUV pulse envelopes. In this way, half of the spectra shown in our manuscript were collected with increasing relative-delay, while the remaining half was collected with decreasing relative delay. These spectra, each collected at a unique value of the relative delay, were joined resulting in the ATR spectrogram presented in the manuscript.

ATI Background Subtraction

The measured electron spectra have a form of two peaks existing on top of a background. This background appears due to two processes. First, the NIR probe field can create electrons with kinetic energies reaching 100 eV, by a process, which is analogous to the above-threshold ionization process (ATI) in isolated atoms. For brevity, we refer to this part of the background as "ATI background." Second, an electron ejected by the extreme-ultraviolet (XUV) pulse can experience inelastic collisions before it leaves the metal. Comparison of photoelectron spectra recorded with and without the presence of the NIR streaking field provides insight into the properties of the XUV-induced ATI background signals. Spectra recorded with and without the presence of the NIR streaking field are shown below in Supplementary Fig. 1.

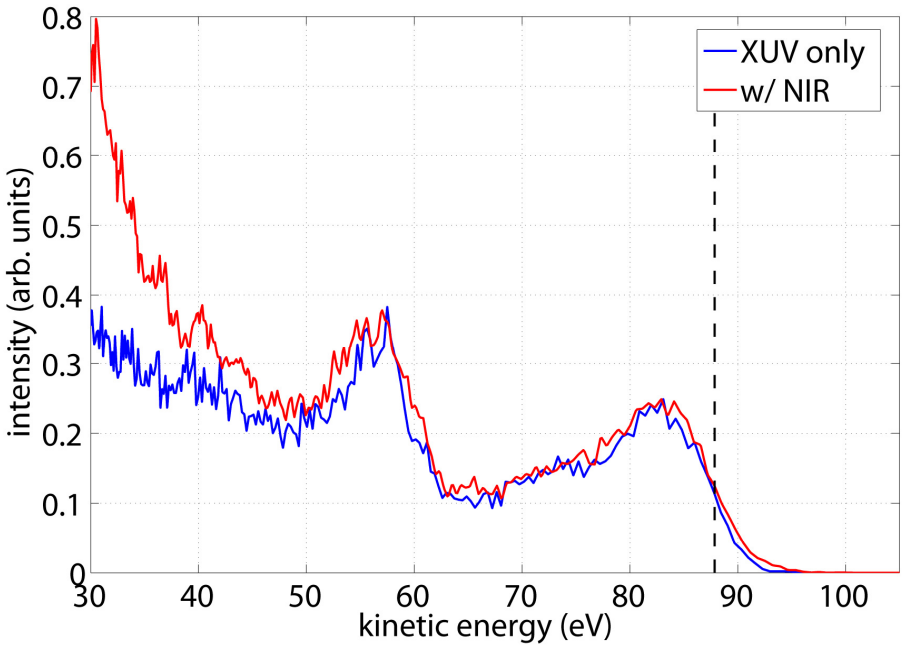

Supplementary Figure 1| Reference spectrum. The blue curve shows a photoelectron spectrum measured without the presence of the probe NIR streaking field using XUV photons of ~91 eV. This XUV-only spectrum has been

shifted to higher energy by ~3eV to compensate for space charge effects. The red curve is a spectrum recorded with the NIR field with the relative-delay set far from time-zero for comparison. The XUV only spectrum is used to identify the background component that is due to ATI. The dashed line marks the kinetic energy for photoelectrons emitted from states at the Fermi energy.

The two distinct background contributions are different in their nature. In particular, the ATI background is not streaked as the delay between the laser pulse and the XUV pulse changes because it appears independent of the XUV radiation. Nevertheless, this part of the background may change from one spectrum to another due to laser fluctuation and appearance of contaminants on the tungsten surface. To make a more accurate analysis of the streaked data, we subtracted this ATI background. To separate it from the XUV-produced background we analyzed the spectral region between 30 and 45 eV (our detector is saturated below 30 eV), in which (i) the ATI electrons make a significant contribution to the spectra, (ii) the ATI spectra decay exponentially with increasing electron energy, and (iii) the XUV-produced background is known from independent laser-free XUV photoemission measurements. Furthermore, we assumed that the deformation of the XUV-produced background due to the streaking field can be neglected (in accordance with our Fourier analysis described later in this document) and used the following procedure to subtract the ATI background:

1. Each measured spectrum $I_k(\varepsilon)$ was fitted with the function $I_k(\varepsilon) = \exp(a_k\varepsilon + b_k) + cI_0(\varepsilon)$ in the range $30 \le \varepsilon \le 45$ eV, where $I_0(\varepsilon)$ is a photoelectron spectrum measured without the laser field. The constants a_k and b_k were allowed to vary for the different spectra while *c* remained fixed.

2. The function, $\exp(a_k\varepsilon + b_k)$, which represents the ATI background in spectrum k, was subtracted from the measured spectral intensity such that $\tilde{I}_k = I_k - \exp(a_k\varepsilon + b_k)$.

For $I_0(\varepsilon)$ we used the spectrum shown in Supplementary Fig. 1 after it was shifted by 3 eV toward higher energies in order to account for the additional electron acceleration due to space-charge created by the NIR streaking field. Space-charge refers to low energy photoelectrons which remain near the metal surface and provide an additional acceleration to the high energy 4*f* and conduction-band photoelectrons. This shift of 3 eV is observed in the location of the inflection point (Fermi energy electrons), as well as in the photoelectron peaks when the NIR laser is turned on and off.

In the context of our attosecond photoelectron spectroscopy, space-charge effects are frozen on the relevant timescale. Indeed, space charge was observed to produce a "DC shift" in the measured photoelectron spectra, but the shape of the emission peaks was preserved.

Fourier Analysis

We use Fourier analysis to study the time-dependent behaviour of the background in our measured ATR spectrograms. Since the time-dependence, as a function of relative delay, of the streaked features in the ATR spectrogram is determined by the vector-potential of the streaking field, we concentrate our attention on the Fourier component at the laser frequency, which we calculate for every value of the electron energy ε:

$$u(\varepsilon) = \int_{\tau_{\min}}^{\tau_{\max}} \left[I(\varepsilon,\tau) - I_{\text{avr}}(\varepsilon) \right] e^{i\omega_L \tau} d\tau \qquad (1.1)$$

where τ is the relative delay, $I(\varepsilon,\tau)$ is the measured spectral intensity, and

$$I_{\mathrm{avr}}(\varepsilon) = \frac{1}{\tau_{\max} - \tau_{\min}} \int_{\tau_{\min}}^{\tau_{\max}} I(\varepsilon, \tau) d\tau \qquad (1.2)$$

is the intensity averaged over the delay. The results of this analysis are summarized below in Supplementary Fig. 2. The magnitude of $u(\varepsilon)$ is maximal at the slopes of the peaks, where a small spectral shift causes the largest change in the spectral intensity. It is clear from this analysis that virtually no periodic modulation at the laser frequency is observed in regions containing only background, specifically at energies below the 4*f* peak or in between the peaks. Therefore, streaking of the XUV-produced background was determined to be negligibly small in the current measurements. Indeed, if the background were shifted by the same magnitude as the 4*f* and conduction-band peaks, then in those regions where the background dominates the signal, the spectral intensity would change periodically with delay.

This static behaviour of the background electrons can be expected for several reasons. Most importantly, streaking can only be observed if the duration of the streaked electron wave packet is sufficiently small. Ideally, the wave packet should be much shorter than the period of the streaking field. While the electrons that compose the photoemission peaks come from the first few atomic layers, the background electrons can be contributed from much deeper in the material, so that they need more time to reach the surface, which broadens their emission time and therefore weakens the effect of streaking.

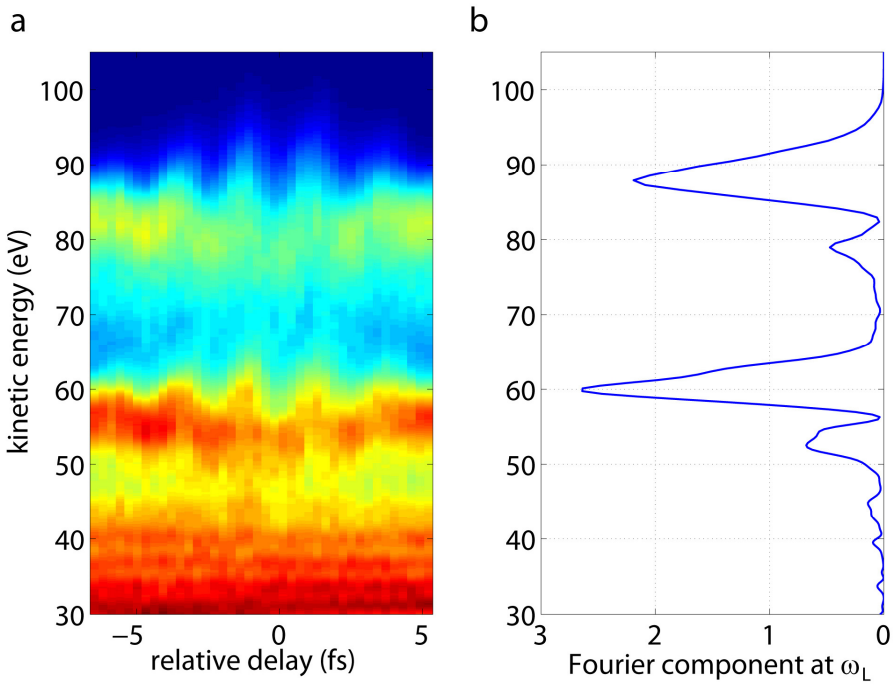

Supplementary Figure 2| Fourier Analysis. The ATI-background subtracted ATR spectrogram reproduced from Fig. 2b in the main text is shown for reference in panel **a**. Fourier analysis of the recorded ATR spectrogram at a fixed frequency (the carrier laser frequency) as a function of measured photoelectron kinetic energy is performed. At energies where the photoelectron intensity is deeply modulated with the laser frequency as a function of relative delay, indicative of streaking, the Fourier component will be large. Conversely, at energies where the photoelectrons are not streaked by the overlapping NIR field the Fourier component will be negligible. The results of this analysis are shown in panel **b**. At the rising and falling edges of the direct emission peaks, strong modulation at the laser carrier frequency exists. However, in between the peaks and at energies below the 4*f* peak, the Fourier components are very small indicating that the background signal intensity is negligibly streaked in comparison to the direct 4*f*-states and conduction-band emission. Consequently, the background is assumed to be independent of the relative delay between XUV and NIR streaking field.

COM Analysis

We measured the time-shift between the 4*f* and conduction-band spectrograms by analyzing the centre-of-mass (COM) of the spectral regions, 47 to 66 eV and 66 to 110 eV, which contain the 4*f* and conduction-band peaks, respectively. As already mentioned in the main text, we believe that the COM is an excellent descriptor of the periodic motion of the peaks because this approach requires no assumptions or fit parameters yet provides access to timing information that is invariant to the laser parameters, and is relatively insensitive to background photoelectrons. Due to the unknown background underlying the 4*f* and conduction-band peaks, the spectrum cannot be fit based on the known band-structure of tungsten.

However, the amplitude of the COM motion of the region containing the peaks is not as large as the motion exhibited by the peaks themselves (the motion of the peak is observed in the false colour plot of Fig. 2b in the original manuscript) owing to the delay-independent background on which they exist. The COM of the spectral region containing the 4*f* peak, which exists on a larger background, is much more strongly damped when compared to the motion of the conduction band region COM. As a result, in the original manuscript Fig. 3b, the COM data points were scaled for ease of visual comparison. This, of course, had no effect on the measured emission delay because we were comparing zero-crossings of the vector potential.

To illustrate how the background can stabilize the COM, let us consider a point mass m moving on a rectangular block of mass M. The centre of mass of this system is given by,

$$\langle x \rangle = \frac{mx}{m+M} = \frac{x}{1+\frac{M}{m}} \qquad (1.3)$$

where x is the position of the point mass m. If we move the point mass by a distance Δx the COM of the full system will be shifted by a smaller value. The COM motion will be reduced as the pedestal mass M is increased. While our previous Fourier analysis shows no indication that the background is streaked, or periodically changing with relative delay, its stabilizing effect would be nearly the same, even if it were to move, because the COM is calculated in a spectral window that fully contains the peak, but only encloses a small part of the background.

Uncertainty Estimate

In order to evaluate the uncertainty in this measured delay, we first estimated the error with which the individual photoelectron spectra and thereby COM were obtained. The 4*f* and conduction-band spectrograms presented in the main text are composed of 40 individual measured spectra $I(\tau,\varepsilon)$, which contain sufficient information to determine standard deviations of the measured spectral intensities. One possible approach to do so is to make a Fourier analysis of the measured spectra, and assume that the high-frequency Fourier components of the signal can be attributed to noise. Having done this we found that the noise level was dominated by the detector shot noise. The average relative error was found to be ~4%.

Having assigned standard deviations $\sigma_I(\tau,\varepsilon)$ to the measured intensities the standard deviation for a COM calculated for a spectrum $I(\tau,\varepsilon)$ within a certain energy range could be calculated as:

$$\sigma_{\mathrm{COM}}(\tau) \approx \sqrt{\sum_i \left(\sigma_I(\tau,\varepsilon_i) \frac{\partial \varepsilon_{\mathrm{COM}}(\tau)}{\partial I} \right)^2} = \frac{\sqrt{\sum_i \left[\sigma_I(\tau,\varepsilon_i)(\varepsilon_i - \varepsilon_{\mathrm{COM}}(\tau)) \right]^2}}{\sum_i I(\tau,\varepsilon_i)} \qquad (1.4)$$

where

$$\varepsilon_{\mathrm{COM}}(\tau) = \frac{\sum_i \varepsilon_i I(\tau, \varepsilon_i)}{\sum_i I(\tau, \varepsilon_i)}. \qquad (1.5)$$

These standard deviations are shown in Fig. 3b of the main paper as vertical error bars. The next step in our analysis is evaluation of the uncertainty in the horizontal shift between the oscillations of the 4*f* and conduction band COM motion as a function of delay. We assign this value of uncertainty to the measured delay between the emission times of the photoelectron wave packets.

To accomplish this, for each of the spectrograms we first found a straight line about which the COM oscillates. If there were no change in the space-charge effect over the course of the entire measurement, this line would be horizontal. To allow for a slight monotonic increase of the electron kinetic energy, due to the slow accumulation of space charge, which is a function of relative delay, we allowed this line to be tilted. In our measurements the total change in the space charge effect over the full range of delay was ~0.1 eV (the average value of the effect was ~3eV). To more precisely determine the slope of the line we fit each of the COM point sets with a function of the form:

$$y(\tau) = u\tau + v + ae^{-\gamma(t-t_L)^2}\cos(\omega_L\tau + \beta\tau^2 + \varphi) \qquad (1.6)$$

After determining the linear offset function we *discarded* this fit and the COM data points were simply connected by linear interpolation to generate the continuous curves $\varepsilon_{\mathrm{COM}}(\tau)$, for the COMs of the two spectral regions containing the 4*f* and conduction-band. These interpolated functions were used to find the intersection of the oscillatory motion of the COM with the linear offset function. The points of intersection of the interpolated curves with the linear offset function are considered to occur at the zero-crossing of the streaking vector potential and are called $\tau^{(4f)}$ and $\tau^{(cb)}$. The time-

delay between the 4*f* and conduction-band spectrograms can be determined independently at each intersection as $\Delta\tau = \tau^{(4f)} - \tau^{(cb)}$ as shown below in Supplementary Fig. 3.

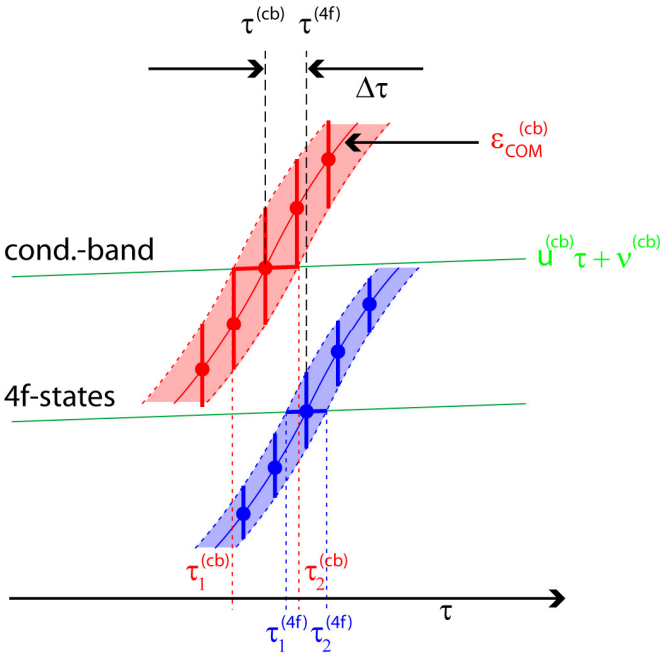

Supplementary Figure 3| Assigning measurement error. Depiction of COM motion of the 4*f* and conduction-band peaks as a function of relative delay τ. Individual COM data points were connected by linear interpolation to generate the smooth curve $\varepsilon_{COM}(\tau)$. We use these curves together with corresponding curves generated from the vertical error bars, which were calculated from noise in the measured spectrum, to obtain values for the uncertainty along the time-delay axis which corresponds to the uncertainty with which we have measured $\Delta\tau$, the shift of the spectrograms.

Similarly, intersection points given by solutions to the equations $u\tau_1 + v = \varepsilon_{\mathrm{COM}}(\tau_1) + \sigma_{\mathrm{COM}}(\tau_1)$, and $u\tau_2 + v = \varepsilon_{\mathrm{COM}}(\tau_2) - \sigma_{\mathrm{COM}}(\tau_2)$, corresponding to curves drawn through the "tops" of the error bars, and the "bottoms" of the error bars,

respectively, provided us with an estimation of the horizontal error bars at the intersections:

$$\sigma_{\Delta\tau} \approx \frac{1}{2}\sqrt{\left(\tau_2^{(4f)} - \tau_1^{(4f)}\right)^2 + \left(\tau_2^{(cb)} - \tau_1^{(cb)}\right)^2} \tag{1.7}$$

Considering each such pair of intersections in the measured spectrogram as an independent measurement of the delay $\Delta\tau$, we averaged them:

$$\Delta\tau = \frac{1}{n}\sum_{k=1}^{n}\Delta\tau^{(k)} \tag{1.8}$$

$$\sigma_{\Delta\tau} = \sqrt{\frac{1}{n}\sum_{k=1}^{n}\left(\sigma_{\Delta\tau}^{(k)}\right)^2} \tag{1.9}$$

The results obtained were $\Delta\tau = 110$ attoseconds and $\sigma_{\Delta\tau} = 70$ attoseconds.

Reconstruction of electron wave packets

To reconstruct a photoelectron wave packet is to determine how different continuum states are populated in time as parts of the photoelectron wavefunction leave the metal surface. In this respect, streaking measurements on metal surfaces are similar to those performed on atomic gases. Without the probe streaking field, a plane wave $\exp(i\boldsymbol{pr})$ provides a good description of a continuum state with a momentum $\boldsymbol{p}$ (atomic units are used throughout this section). If the streaking field is present, the plane waves must be replaced with Volkov states:

$$\psi_p(y,t) = e^{ipy}e^{-\frac{i}{2}\int_0^t [p-A(t')]^2\,dt'} \tag{1.10}$$

where $A(t)$ is given by

$$A(t) = \int_t^\infty E(t')dt' \tag{1.11}$$

and $E(t)$ is the component of the NIR streaking field which points toward the photoelectron detector.

In comparison to atomic gases, a theoretical description of a streaking measurement on a metal surface presents many additional challenges. First, the initial states are represented by energy bands (in contrast to isolated energy levels in the case of a single atom). Second, if strong enough, the laser field can significantly affect the electrons in the conduction band populating previously unoccupied states and possibly distorting the band structure. Third, an electron can experience an inelastic collision on its way out of the metal. Fourth, the streaking field creates space-charge at the metal surface.

In our first attempt to reconstruct electron wave packets launched on a metal surface we address these challenges by introducing several approximations and acknowledge that further work is necessary to develop more accurate models. First, we neglect the effect of the streaking field on the initial states. This is justified because, in our experimental geometry, the NIR field inside the crystal predominantly accelerates conduction-band electrons along the metal surface, while the time-of-flight detector was set up to detect electrons propagating along the surface normal. Second, we assume that streaking of the XUV-produced background can be neglected, which is supported by our Fourier analysis. Therefore, we define the background as the delay-independent part of the streaked spectra:

$$\sigma(p,\tau) = \sigma_b(p) + \sigma_s(p,\tau) \tag{1.12}$$

where p is the momentum, τ is the delay, σ_b is the background, and σ_s represents the streaked "signal."

Our model of the streaking measurement also includes the possibility of jitter in the delay between the XUV pulse and NIR streaking pulse. This jitter can have several sources. When the XUV and the laser pulses are split and delayed with respect to each other, their relative delay can change due to mechanical vibrations. Instability of the carrier-envelope-offset (CEO) phase of the laser pulse can also contribute to the jitter, though this is a secondary effect because the harmonic emission is locked to the phase of the laser field, independent of the pulse envelope. Finally, electron wave packets launched from different atomic layers can arrive at the surface at different times with respect to each other. For our first proof-of-principle simulations we chose to describe the cumulative effect of all the jitter sources by a single parameter:

$$\sigma_s(p,\tau) = \int_{-\infty}^{\infty} \sigma_0(p,\tau') e^{-\frac{(\tau'-\tau)^2}{T_{jitt}^2}} d\tau' \qquad (1.13)$$

where T_{jitt} determines the jitter strength.

The spectrum $\sigma_0(p,\tau)$ is the photoemission spectrum in the absence of jitter and streaking. In the present experiment this spectrum is assumed to be a sum of three components, two contributions are due to the $4f_{5/2}$ and $4f_{7/2}$ states, and the remaining contribution is due to the conduction band:

$$\sigma_0(p,\tau) = \sigma_{4f1}(p,\tau) + \sigma_{4f2}(p,\tau) + \sigma_{cb}(p,\tau) \qquad (1.14)$$

The $4f$ states are considered to be localized, therefore, we use the same streaking model as that used for isolated atoms:

$$\sigma_{4f1}(p,\tau) = \left| \int_{-\infty}^{\infty} dt\, f_{4f}(t+\tau) e^{-i\varepsilon_{4f1}t} e^{\frac{i}{2}\int_0^t [p+A(t')]^2 dt'} \right|^2, \qquad (1.15)$$

$$\sigma_{4f2}(p,\tau) = 1.6 \left| \int_{-\infty}^{\infty} dt\, f_{4f}(t+\tau) e^{-i\varepsilon_{4f2}t} e^{\frac{i}{2}\int_0^t [p+A(t')]^2 dt'} \right|^2, \qquad (1.16)$$

where ε_{4f1} and ε_{4f2} are kinetic energies of the wave-packets in the absence of the streaking field ($\varepsilon_{4f2} - \varepsilon_{4f1} = 2.18$ eV spin-orbit splitting), and the factor of 1.6 represents the branching ratio of the two channels[4]. The function $f_{4f}(t)$ in these equations is the complex-valued probability amplitude describing both 4*f* wave packets.

For the spectra of electrons launched from the conduction band $\sigma_{cb}(p,\tau)$ we used the following model:

$$\sigma_{cb}(p,\tau) = a_{cb}\int_{-\infty}^{\infty} dp'\, e^{-\frac{(p-p')^2}{\Delta p^2}} \left| \int_{-\infty}^{\infty} dt\, f_{cb}(t+\tau+\Delta\tau) e^{-i\varepsilon_{cb}t} e^{\frac{i}{2}\int_0^t [p'+A(t')]^2 dt'} \right|^2, \qquad (1.17)$$

where the term $\exp[-(p-p')^2/\Delta p^2]$ models the spectral broadening due to the finite depth of the conduction-band Δp, the function $f_{cb}(t)$ describes the conduction-band wave packet, and $\Delta\tau$ introduces a possible delay between the emission of the conduction-band wave packet and the 4*f* wave packets.

The goal of our reconstruction is to retrieve the functions $f_{4f}(t)$ and $f_{cb}(t)$. In particular, we would like to know the duration and the chirp of the excited electron wave packets, and we would also like to know if these wave packets are launched simultaneously or delayed with respect to each other. To simplify the reconstruction, we assumed that the 4*f* and conduction band wave packets can be approximated by Gaussian functions of the same duration, which would be limited by the duration of the exciting XUV pulse, but allowed them to vary in their quadratic phase, or chirp:

$$f_{4f}(t) = e^{-\frac{t^2}{T^2} + i\beta_{4f}t^2}, \qquad (1.18)$$

$$f_{cb}(t) = e^{-\frac{t^2}{T^2} + i\beta_{cb}t^2}. \qquad (1.19)$$

To model the streaked spectra one needs to know the field of the streaking laser pulse. This information can be obtained from the streaked spectra themselves. We used the following parameterization of $A(t)$:

$$A(t) = A_0 e^{-\gamma(t-t_L)^2} \cos(\omega_L t + \varphi_L) \qquad (1.20)$$

where γ determines the duration of the pulse, t_L is the position of the peak of the envelope, ω_L is the laser frequency, and φ_L is the CEO phase.

Reconstruction results

To determine the values of the parameters that best describe the wave packets and the streaking field, we used them as optimization parameters in a procedure that attempts to minimize the difference between the measured and the reconstructed spectra. Table 1 contains the retrieved values of the most important parameters. While our method does not allow us to put uncertainty limits on the retrieved values, it gives estimates for the electron wave packet durations that are reasonable considering the bandwidth of the XUV mirror reflectivity, and best agreement with the measured data is achieved for a value of $\Delta\tau \sim 100$ as in agreement with our observation by COM analysis as already noted in the main text.

Supplementary Figure 4 shows the reconstructed vector potential of the streaking NIR laser pulse. Based on this reconstruction, the NIR streaking field strength was found to be E_y=3.2x10^9 V/m. Using this value and the classical model of refraction at a metal surface, we found that the amplitude of the incident laser field was equal to E=1.2E_y, which corresponds to the intensity 2x10^{12} W/cm^2 and is in agreement with an experimental estimate made based on the incident pulse energy, pulse duration, focal length of the focusing mirror and area illuminated on the focusing mirror. Additionally, in Supplementary Fig. 4, four positions of overlap between the XUV and NIR streaking

field are marked with red circles. Measured and reconstructed photoemission spectra collected at these overlap positions are shown in Supplementary Fig. 5. Three of the spectra shown in Supplementary Fig. 5 are close to either a peak or a zero-crossing of the vector potential where most of the information about the streaked wave packet is obtained. The fourth panel in Supplementary Fig. 5 shows a spectrum collected far from the peak of overlap and is displayed for reference.

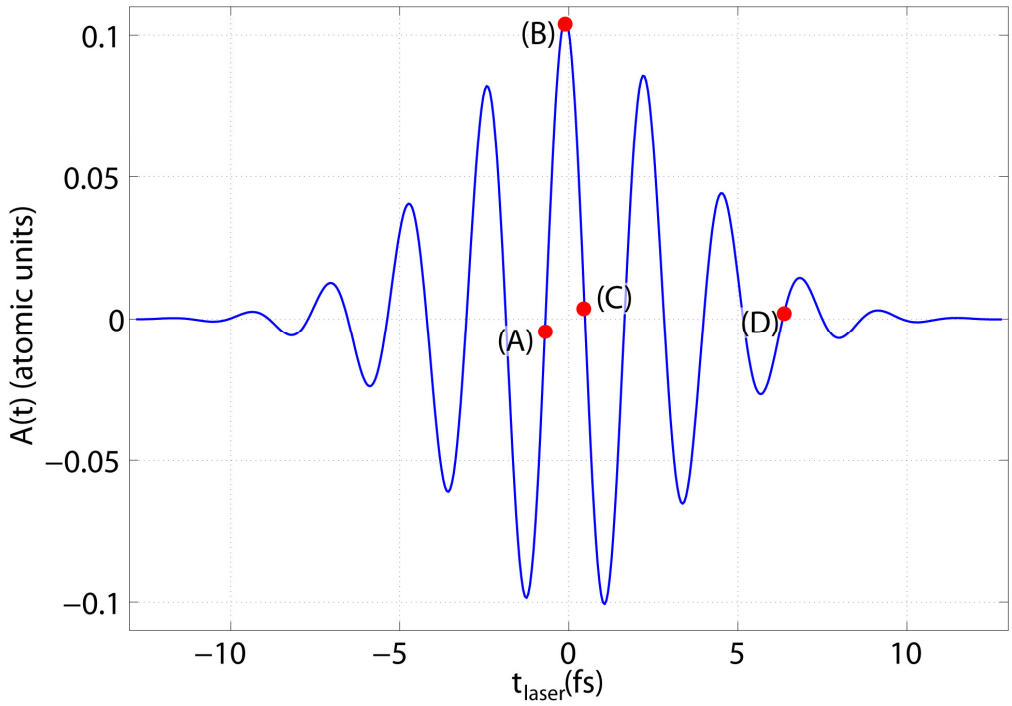

Supplementary Figure 4| Streaking waveform. Reconstructed vector potential of the streaking laser pulse. The positions “A”, “B”, “C”, and “D” mark individual positions of overlap between the XUV and streaking pulse for the photoemission spectra shown in Supplementary Fig. 5. (In this figure, the time axis is an absolute coordinate rather than the relative delay between the XUV and laser pulse, which is used in the main text. The coordinates are related by the expression, $\tau = t_{laser} - t_{xuv}$, where t_{laser} and t_{xuv} are measured from the maximum of the respective pulse envelope.)

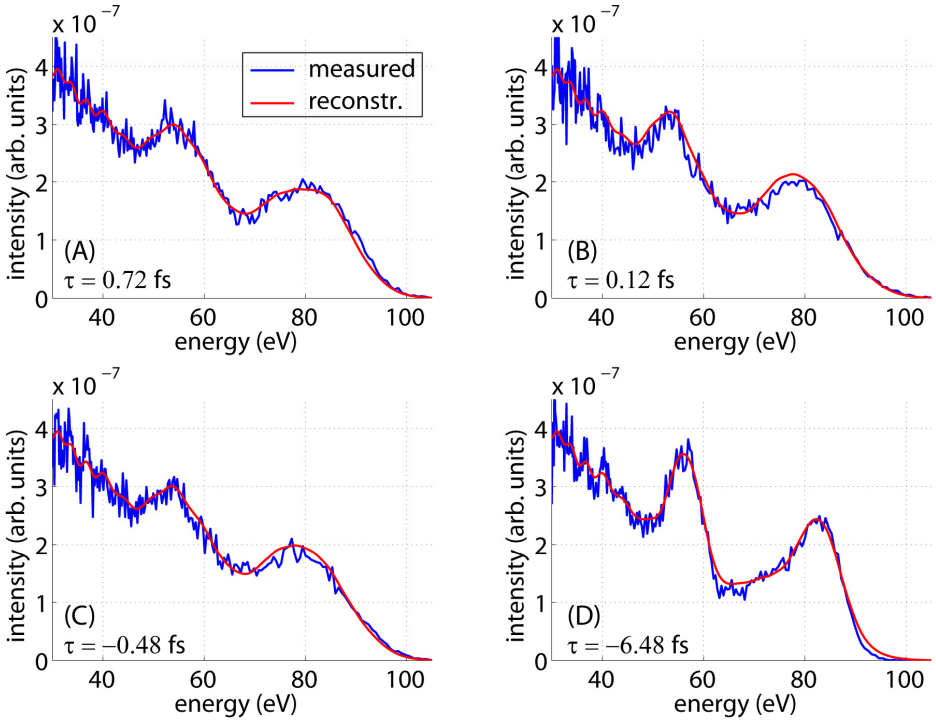

Supplementary Figure 5| ATR reconstruction. Photoelectron spectra collected at four different overlap positions ("A", "B", "C", and "D") of the XUV and streaking pulse as indicated in Supplementary Fig. 4. The value of the relative delay, τ, is also indicated in each panel.

Supplementary Table 1| Important parameters obtained by reconstruction of the measured ATR spectrograms.

FWHM of the wave packets	0.29 fs
β_{4f}	-5.2 fs^{-2}
β_{cb}	-8.9 fs^{-2}
band broadening Δp (atomic units)	0.067
FWHM of the laser pulse	5.7 fs
A_0 (atomic units)	0.11
laser wavelength $\lambda_L = 2\pi c / \omega_L$	702 nm
delay $\Delta\tau$ between the wave-packets	0.102 fs

Tungsten band structure

To describe the electronic structure of single-crystal tungsten in which transport of the detected photoelectrons occur, Supplementary Fig. 6 shows the static band structure of bulk body-centered cubic (bcc) tungsten (W) along the Γ → N direction. This is the direction corresponding to the surface normal of the W (110) face, which corresponds to the attosecond photoemission experiment described in the main text. The band structure shown in Supplementary Fig. 6 was calculated by employing the full-potential linearized augmented plane wave method[5] as implemented in the FLEUR code[6]. These calculations have used the experimentally determined lattice constant of W, a = 3.165 Å. The energies given are in reference to the Fermi level of tungsten as opposed to in the main text where observed photoelectron kinetic energies are given. In this convention, the energy regions of the upper-conduction bands involved in our studies of

photoelectrons from the 4*f* core states and from the conduction band are centred about 58 eV and 85 eV, respectively. The regions of interest in the calculated W band structure diagram are shaded in Supplementary Fig. 6. These shaded regions show the upper-conduction bands in which the photoelectrons may propagate towards the surface. The Bloch state group velocity of an electron in a conduction band is proportional to the derivative of the energy band with respect to the momentum wave-vector *k*. Therefore, electrons which exist in more steeply shaped conduction bands will have a higher Bloch state group velocity.

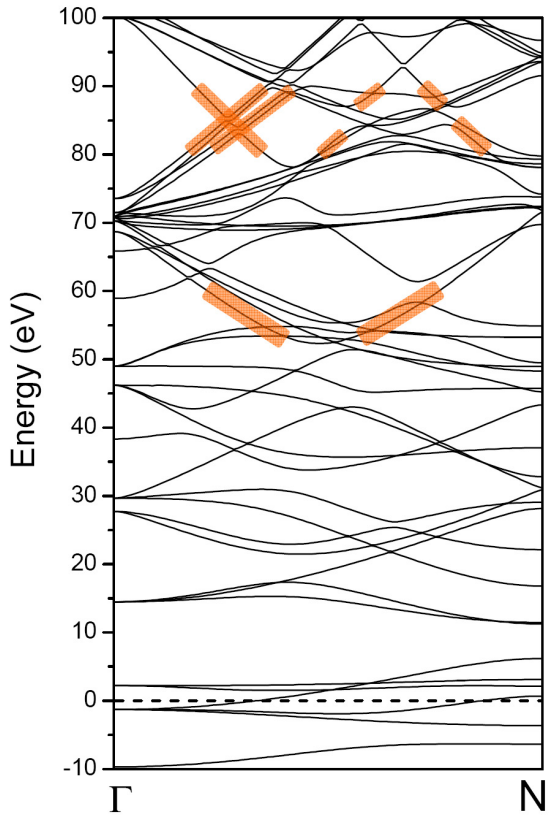

Supplementary Figure 6: Tungsten band structure. Band structure calculation of body-centered cubic tungsten along the Γ → N direction of bulk momentum (normal to (110) surface). Zero on the energy axis is defined by the Fermi energy. Electrons from the 4*f* states are photoexcited by a ~91eV XUV

photon into the upper conduction bands that are shaded and centered about 58 eV. Similarly, electrons from the conduction band are photoexcited to the upper conduction bands centered about 85 eV. The slope of these upper conduction bands can be used to estimate the velocity of the photoelectron as it is transported to the crystal surface.

Supplementary Figure 7 shows a calculation of the corresponding group velocities along $\Gamma \rightarrow$ N as a function of the energy. The result is displayed as points for all individual bands shown in Supplementary Fig. 6. It is clear that the envelope of these points does not coincide with the free electron model, which would have resulted in a parabola-shaped envelope. The velocities of *free electrons* with kinetic energies of 85 eV and 58 eV would be 5.5×10^6 m/s and 4.5×10^6 m/s, respectively, yielding a velocity ratio between the free-electrons of 1.2. However, the mean velocities for photoelectrons in W (110) excited from the conduction band states and from the 4*f* core-state is actually calculated to be about 6.5×10^6 m/s and 3.6×10^6 m/s, respectively, corresponding to a ratio of 1.8, which is 50% higher than that for free electrons.

It should be noted that these values are approximate, as no selection rules and no transition probabilities for the individual transitions have been taken into account. Furthermore, surface effects are not included in the group velocity calculations. It is also unclear that static W band structure calculations can be used directly to describe the transient electronic structure of the upper band in the very first few attoseconds following the XUV excitation. Despite these limitations, we currently rely on this description, as a full theoretical treatment of the time dependent photoemission process is currently unfeasible.

In summary, electrons of ~85 eV kinetic energy need about 60 as to propagate a distance of 0.4 nm in the crystal while electrons of ~58 eV need 150 as to propagate 0.5

nm distance, leading to an estimated delayed emission of 90 as in good agreement with our experimental findings.

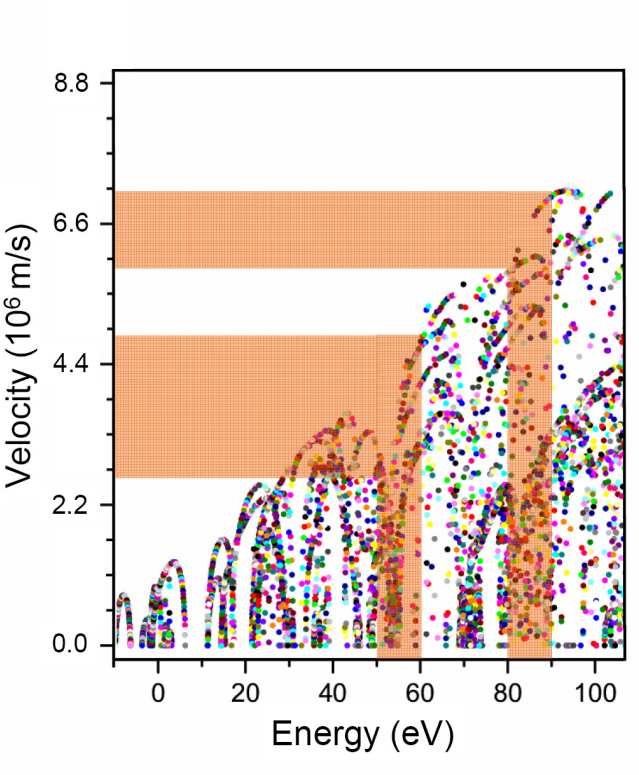

Supplementary Figure 7| Tungsten upper-conduction band group velocities. Velocity calculations for electrons existing in all conduction bands shown in Supplementary Supplementary Fig. 6 (selection rules are not taken into account). The shaded areas describe the highest possible group velocities of wave packets in the upper conduction bands accessible by photoexcitation from the 4*f* core states and the conduction band near the Fermi energy using ~91 eV XUV radiation. All energies are given in reference to the Fermi energy.

References:

1. Baltuska, A. *et. al.* Attosecond control of electronic processes by intense light fields. *Nature* **421**, 611-615 (2003).

2. Baltuska, A. *et. al.* Phase controlled amplification of few-cycle laser pulses. *IEEE J. Sel. Top. Quant. Electron.* **9**, 972-989 (2003).

3. Kienberger, R. *et. al.* Atomic transient recorder. *Nature* **427**, 817-821 (2004).

4. Rose, H. B. *et al.* Spin-orbit-induced spin polarization in W 4*f* photoemission. *Phys Rev. B* **53**, 1630-1634 (1996).

5. Wimmer, E., Krakauer, H., Weinert, M. & Freeman, A. J. Full-potential self-consistent linearized-augmented-plane-wave method for calculating the electronic-structure of molecules and surfaces – O2 molecule. *Phys. Rev. B* **24**, 864-875 (1981).

6. Welcome to the FLEUR code. http://www.flapw.de/